

We are IntechOpen, the world's leading publisher of Open Access books Built by scientists, for scientists

6,900

Open access books available

186,000

International authors and editors

200M

Downloads

Our authors are among the

154

Countries delivered to

TOP 1%

most cited scientists

12.2%

Contributors from top 500 universities



WEB OF SCIENCE™

Selection of our books indexed in the Book Citation Index
in Web of Science™ Core Collection (BKCI)

Interested in publishing with us?
Contact book.department@intechopen.com

Numbers displayed above are based on latest data collected.
For more information visit www.intechopen.com



Nanogenerators from Electrical Discharge

Jie Wang, Di Liu, Linglin Zhou and Zhong Lin Wang

Abstract

Electrical discharge is generally considered as a negative effect in the electronic industry and often causes electrostatic discharge (ESD) and thus failure of electronic components and integrated circuits (IC). However, this effect was recently used to develop a new energy-harvesting technology, direct-current triboelectric nanogenerator (DC-TENG). In this chapter, its fundamental mechanism and the working modes of the nanogenerator will be presented. They are different from the general alternating current TENG (AC-TENG) invented in 2012, which is based on triboelectrification and electrostatic induction. Taking advantage of the electrostatic discharge, it can not only promote the miniaturization trend of TENG and self-powered systems, but also provide a paradigm shifting technique to in situ gain electrical energy.

Keywords: electrostatic discharge, mechanical energy harvesting, nanogenerators, self-powered systems

1. Introduction

Static electricity is a documented phenomenon since the ancient Greek era of 2600 years ago [1–3]. At that time, people found that the amber through friction can attract lightweight particles, attracting a lot of researchers to study the physical principle behind this interesting phenomenon. Triboelectrification (or contact electrification), which refers to the charge transfer between two surfaces in contact, is the principle behind natural phenomena such as the amber effect and lighting [4–8]. Generally, two different materials will have net negative and positive charges, respectively, after contact or by friction based on their capability of gaining and losing electrons. The material which has strong capability of losing electrons will easily be positively charged, and the other has the tendency to be negatively charged. The presence of triboelectric charges on the surface of dielectric will build a strong electric field. When two materials of different polarities are close to each other, a charged material close to either a metal or ground, the electrostatic field between the two materials may break down the air and finally form electrical discharge.

Electrostatic discharge is a ubiquitous phenomenon in our daily life which is a sudden flow of electricity between two charged materials caused by contact or dielectric breakdown [9–13]. For instance, during dry winters, the body easily accumulates static electricity, and it is very prone to discharge when it makes contact with conductors or other people. Generally, electrical discharge is considered as a negative effect in the electronic industry and often causes electrostatic discharge (ESD) failure of electronic components and integrated circuits (IC). Intensive work has been dedicated to avoiding ESD to protect electronic components and instruments' safety [14–20].

With the rapid development of science and technology, the structure of energy demand has changed dramatically. Conventional ordered energy cannot fully meet modern society's demand of a clean and sustainable power source with the increasing demand of wearable electronics and Internet of Things (IoTs). We need "disordered energy" to meet the remaining energy demand of electronics, which are widely distributed, possibly moved and large quantity [21]. At present, most electronic devices are powered by batteries and/or local power generators. However, a battery has limited life cycle which has to be constantly monitored, recharged, or replaced, and it needs a lot of manpower and material resources, thus increasing the maintenance cost [22]. With considering the working status of each electronics, a variety of energy-harvesting methods show their respective characteristics. For example, solar cells can harvest solar energy except in the day time when there is sun light [23]; wind power generation [24] works under abundant wind energy; a thermal generator can convert temperature difference into electricity [25]; and piezoelectric nanogenerators can convert tiny physical deformations into electricity to self-power small-scale devices [26]. Based on the triboelectrification effect and electrostatic induction, the use of triboelectric nanogenerators (TENGs) has been demonstrated as a cost-effective, clean, and sustainable strategy to convert mechanical energy into electricity with comprehensive advantages of light weight, small size, a wide choice of materials, and high efficiency even at low frequencies [27–30].

2. Triboelectric nanogenerators

In 2012, triboelectric nanogenerators (TENGs) based on triboelectrification effect and electrostatic induction were invented by Zhong Lin Wang to harvest mechanical energy from ambient environment [31]. In addition, the self-powered systems based on TENGs demonstrated an effective solution to supply energy for micro/nano electronics. A conventional TENG can generate AC by the friction of two materials with different electron affinity, where charge transfer occurs between the two surfaces of materials, and then inducing electron transfer between two back electrodes under the periodical mechanical force. Recent research indicates that its fundamental theory lies in Maxwell's displacement current and change in surface polarization [32]. Based on this principle, four different modes of TENGs are built according to different device structures and working environments: vertical contact-separation mode, lateral sliding mode, single-electrode mode, and freestanding triboelectric-layer mode (**Figure 1**) [33]. Based on the four modes of TENG, several works have demonstrated that TENGs can harvest various forms of mechanical energy, such as human motion, vibration, wind and even blue energy, making possible their applications in wearable electronics, remote and mobile environmental sensors, and IoTs [34–38].

As an energy harvester, the output power density is one of the key properties to measure the output capability of TENGs. Recent progress indicates that the power density is quadratically related to triboelectric charge density [39, 40], and thus, great efforts have been concentrated on increasing the triboelectric charge density by means of material improvement, structural optimization, surface modification, and so on [41–43]. Jie Wang et al. fabricated a flexible TENG with the silicon rubber as a triboelectric layer and a mixture of silicon rubber [44], carbon black, and carbon nanotubes as a triboelectric electrode. With optimized structural design, the triboelectric charge density is increased up to $250 \mu\text{C m}^{-2}$. By designing a three-layer TENG, the triboelectric charge density increases to $\sim 270 \mu\text{C m}^{-2}$, which is the theoretical limit of air breakdown [45]. Then, a high-vacuum environment was adopted to suppress electrostatic breakdown and a triboelectric

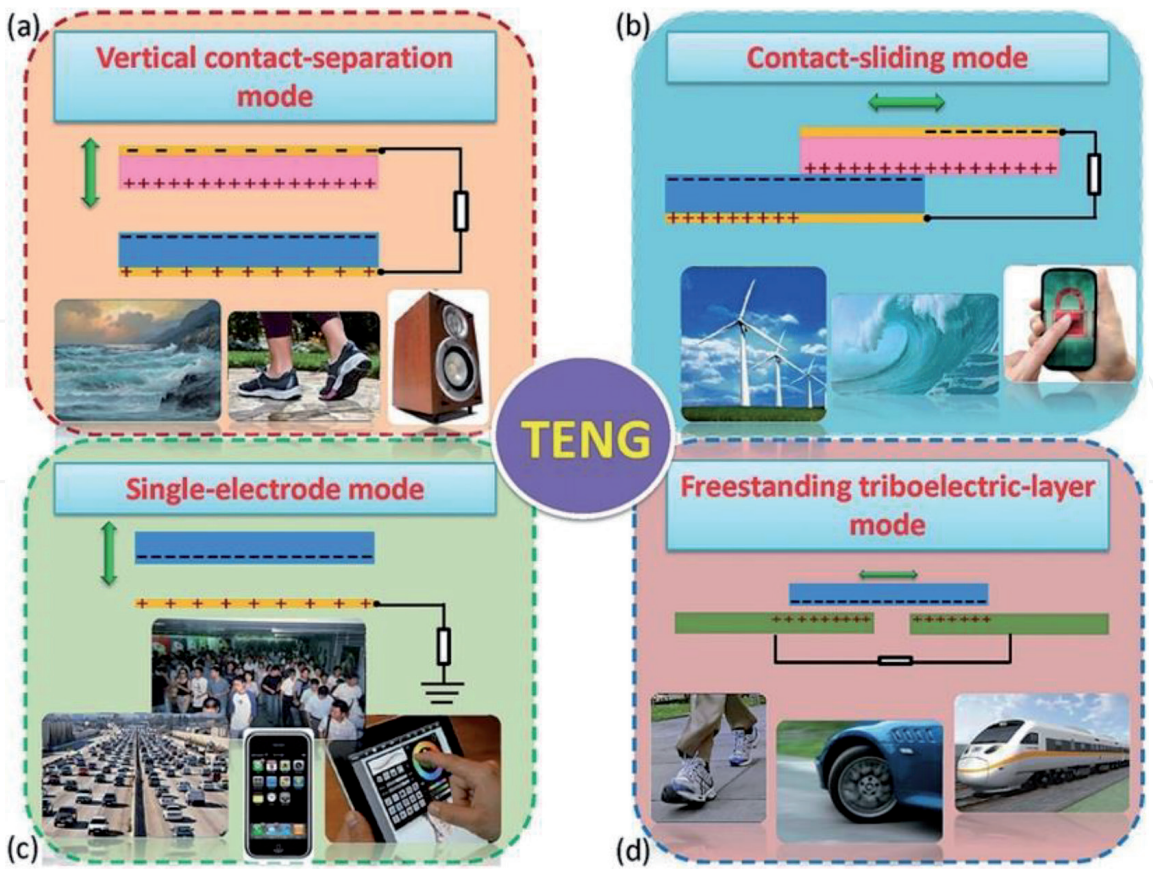


Figure 1.
The four fundamental modes of TENGs: (a) vertical contact-separation mode, (b) in-plane contact-sliding mode, (c) single-electrode mode, and (d) freestanding triboelectric-layer mode [33].

charge density of $660 \mu\text{C m}^{-2}$ is achieved. By further coupling surface polarization from triboelectrification and hysteretic dielectric polarization from ferroelectric material in vacuum, the triboelectric charge density boosts to $1003 \mu\text{C m}^{-2}$ without the constraint of air breakdown [46].

Triboelectric charge density as one of the main optimization directions of TENGs is gradually increased from 50 to $\sim 1000 \mu\text{C m}^{-2}$, and electrostatic breakdown becomes a problem that must to be considered. Generally, a high electrostatic field will be built between the two charged surfaces with opposite triboelectric charges during the working process of TENG. Paschen's law describes the empirical relationship between gaseous breakdown voltage (V_b), gap distance (x), and gas pressure (P) and is given by

$$V_b = \frac{APd}{\ln(Pd) + B} \tag{1}$$

where A and B are constants determined by the composition and the pressure of the gas. For air at standard atmospheric pressure (atm, i.e., the conventional operation condition of a TENG), $A = 273.75 \text{ V Pa}^{-1} \text{ m}^{-1}$ and $B = 1.08$.

According to the theoretical derivation, the gap voltage between contact surfaces of a TENG (V_{gap}) under short-circuit condition is given by

$$V_{\text{gap}} = \frac{\sigma td}{\epsilon_0(t + d\epsilon_r)} \tag{2}$$

where t is the thickness of the polytetrafluoroethylene (PTFE) film, σ the triboelectric surface charge density, ϵ_r the relative permittivity of PTFE ($\epsilon_r \sim 2.1$), and ϵ_0 the vacuum permittivity ($\epsilon_0 \sim 8.85 \times 10^{-12} \text{ F m}^{-1}$).

To avoid air breakdown, V_{gap} must be smaller than V_b at any operation gap distance. Large efforts have been dedicated to study the electrostatic breakdown of TENGs.

3. The confirmation and study of air breakdown in TENG

Using the ion-injection method for introducing surface charges into the dielectric layer, the power density of TENG greatly increases to $\sim 315 \text{ W m}^{-2}$ [39]. With the help of this method, the maximum surface charge density of TENG with the limitation of electrostatic breakdown was observed and confirmed for the first time. As shown in **Figure 2a**, the maximum surface charge density gradually increased with the ion-injection process (the thickness of the utilized FEP film is $50 \mu\text{m}$). In the initial state, the surface charge density only generated by triboelectrification is nearly $50 \mu\text{C m}^{-2}$. Subsequently, step-by-step ion injection was adopted for effective accumulation of the negative charges on the FEP surface, and it is very important to connect the FEP's bottom electrode to the ground in each ion-injection step. After a few ion injections, the surface charge density increased to $\sim 240 \mu\text{C m}^{-2}$ (**Figure 2b**). After the ninth injection, the performance of transferred charges became distinctively different that this abrupt decrease of surface charge resulted from air breakdown. The schematic and numerical simulation results showing the voltage drop in the air gap between the Al and FEP layers, which could cause the air breakdown is shown in **Figure 2c**. This provides a new optimization direction for realizing high output performance of TENG.

After confirming the existence of air breakdown, many researchers studied the electrostatic breakdown of TENGs and various experiments demonstrated the

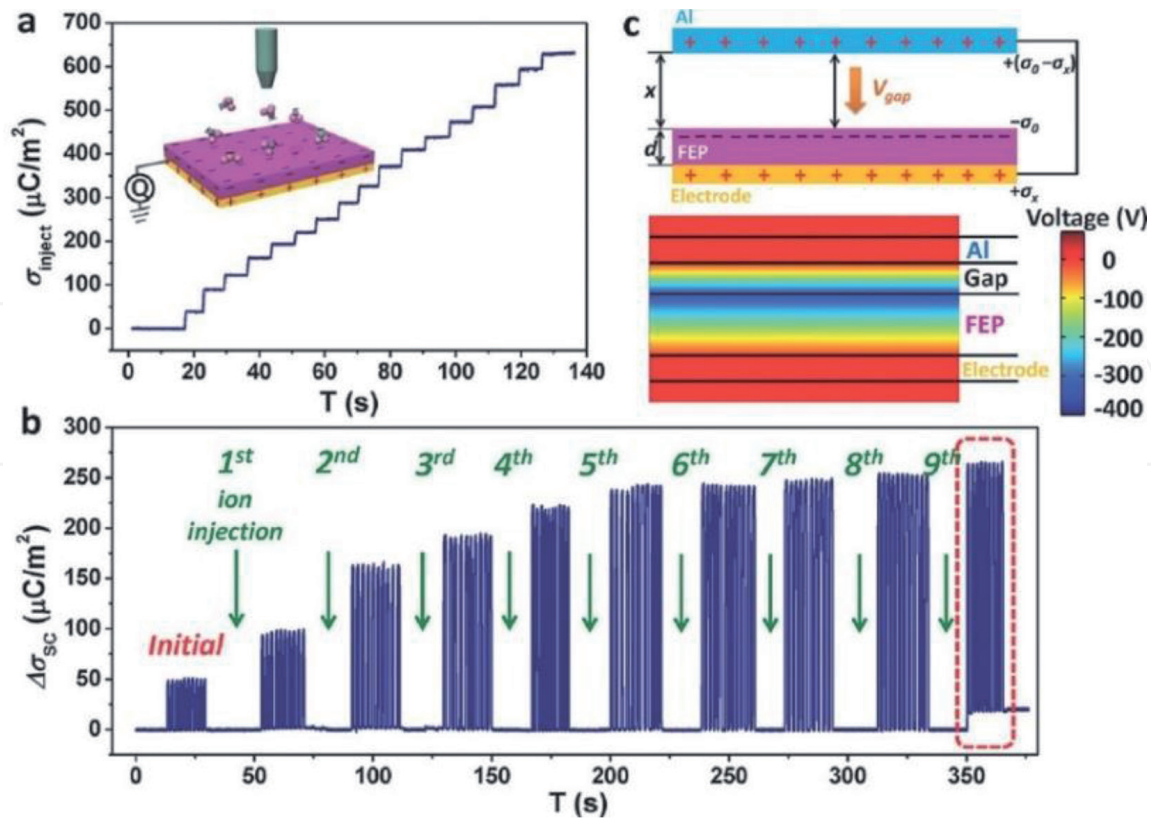


Figure 2. Step-by-step measurement of the surface charge density by ion-injection process. (a) In situ measurement of the charge density of the FEP film during the step-by-step ion-injection process. (b) The short-circuit charge density ($\Delta\sigma_{\text{sc}}$) measured by the TENG when the FEP film was injected with ions time-by-time. (c) Schematic and numerical simulation results showing the voltage drop (V_{gap}) between the Al and the FEP layers, at which the air breakdown may occur [39].

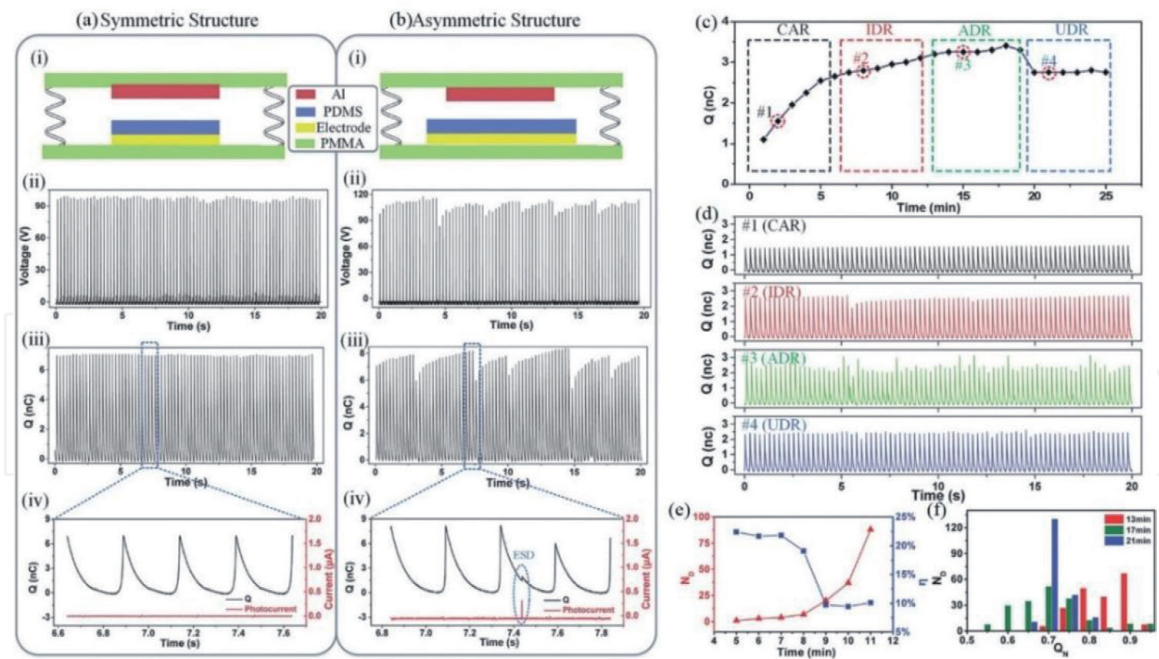


Figure 3. Comparison of S-TENG with A-TENG, and the demonstration of ESD. (a) The structure (i), stable output voltage (ii), stable Q waveforms (iii), and signals detected by a photocurrent detector of S-TENG (iv). (b) The structure (i), abrupt voltage decline (ii), abrupt declined Q waveforms (iii), and signals detected by a photocurrent detector of A-TENG (iv). (c) Triboelectric charges in four different regions of ESD processes. (d) Picked-up, 20-s waveforms for each marked point in (c). (e) ND and η change with time in IDR. (f) Double-layer feature in three different minutes of ADR [47].

existence of air breakdown. Haixia Zhang et al. [47] fabricated a symmetric structure and an asymmetric structure of TENG, discovered the phenomenon of electrostatic breakdown in the asymmetric structure, and then studied the four steps of electrostatic breakdown in detail. **Figure 3a, b** shows the comparison of the symmetric structure and the asymmetric structure. A low-dark-current photoelectric detector is used to test photocurrent signals and an obvious light signal can be observed between the abrupt output decline in **Figure 3b(iv)**, while no light signal has been detected in **Figure 3a(iv)**. The transition process of electrostatic breakdown has been investigated and summarized, and the changes in triboelectric charges with time at four different regions in electrostatic breakdown, which are charge accumulation region (CAR), intermittent discharge region (IDR), accelerated discharge region (ADR), and uniform discharge region (UDR) are shown in **Figure 3c–f**. Meanwhile, the influence of several factors including contact materials, contact pressure, tilted angle, and surface morphology on electrostatic breakdown has been studied.

Yunlong Zi et al. [48] confirmed that the threshold surface charge density of contact-separation mode TENG is nearly $40\sim 50 \mu\text{C m}^{-2}$ with the existence of air breakdown by the theoretical study of the maximized effective energy output, and then the effects of gas pressure (higher than the atmosphere) and gas composition were also studied. **Figure 4a** shows the breakdown voltage as calculated by Paschen's law in 1 atm air, in which the points A–E show the voltage V_1 between triboelectric surfaces of contact-separation mode TENG under different transferred charges. The potential distribution of A–D is simulated by COMSOL Multiphysics software shown in **Figure 4b**. In **Figure 4c,d** are shown the voltage V_1 between the two triboelectric surfaces and the breakdown voltage V_b . To further clearly explain the relationship of V_1 and V_b , **Figure 4e** shows the distribution of $V_b - V_1$ in a V-Q plot with the contour line of 0 V displayed as the red dashed line. The negative (“–”) and positive (“+”) areas are divided by this contour line. They also did experiments to demonstrate the existence of air breakdown. **Figure 4f** is the

mechanism of contact-separation mode TENG when the air breakdown existed. The final charge densities of six TENGs with different initial charge densities are shown in **Figure 4g**. The decrease in final charge densities of TENG #3–6 indicates the existence of air breakdown.

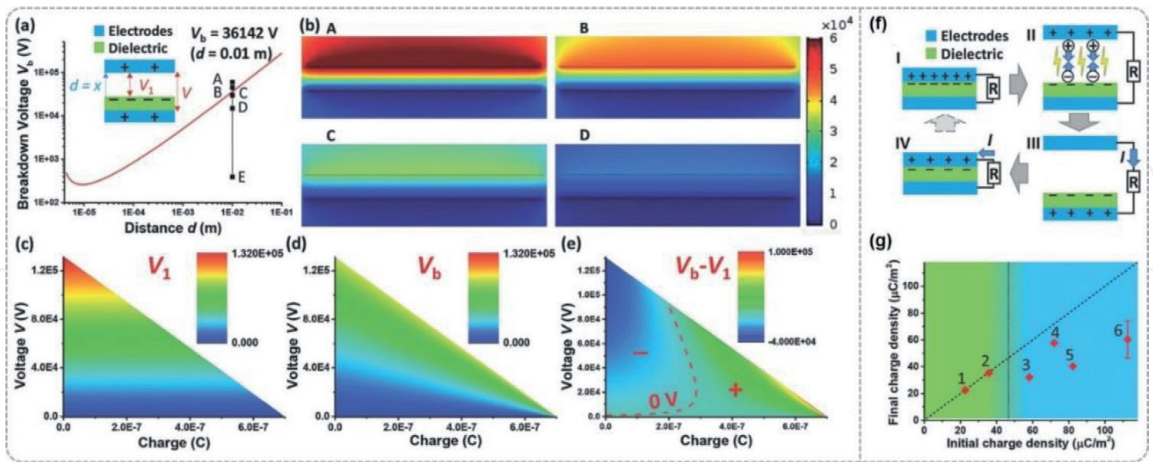


Figure 4. The demonstration of air breakdown in a CS mode TENG. (a) The breakdown voltage calculated by Paschen’s law in 1 atm air, in which the points A–E show the voltage V_1 between dielectric layer and upper electrode of the CS mode TENG with different surface charge density (inset shows the schematic diagram of the TENG). (b) The potential distribution of A–D simulated by COMSOL Multiphysics software. (c) The voltage V_1 between the dielectric layer and upper electrode in V-Q plot. (d) The breakdown voltage V_b in V-Q plot. (e) The distribution of $V_b - V_1$ in V-Q plot. The red dashed line is the contour line of 0 V. (f) The working process of CS mode TENG with air breakdown and the mechanism of the final charge density measurement. (g) The test results of final charge densities for six TENGs. The equal initial and final charge densities are shown with the dashed inclined line, and the dotted vertical line indicates the existence of air breakdown where σ_f separates with σ_o (blue) [48].

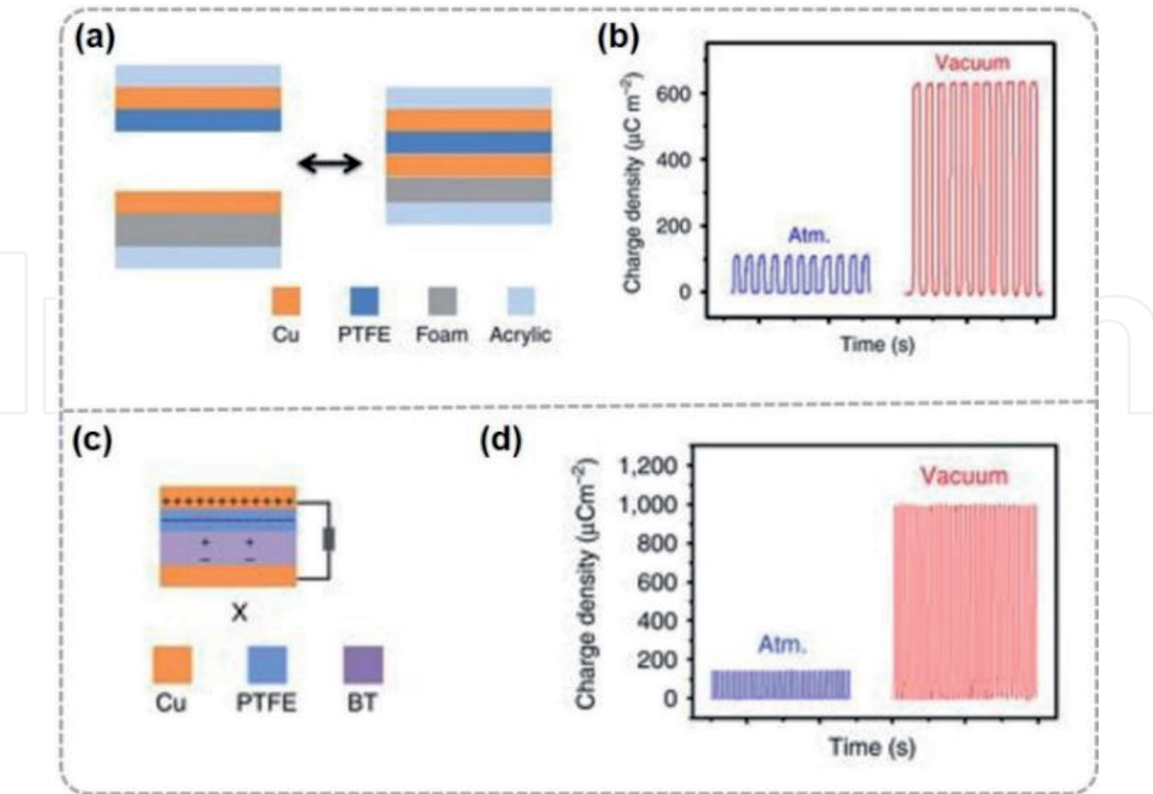


Figure 5. Output performance of TENG in vacuum. (a) Schematic of TENG with a cushioned Cu electrode to increase contact intimacy during operation process. (b) Charge density of the TENG in atmosphere and high vacuum ($P \sim 10^{-6}$ torr). (c) Schematic of the TENG with the integration of triboelectric material (PTFE) with ferroelectric material (BT). (d) Charge density of the TENG in atmosphere and high vacuum [46].

Besides the relatively theoretical research of air breakdown, great efforts have been devoted to suppress or avoid air breakdown for substantially enhancing the output performance of TENGs [49, 50]. On the basis of soft contact and fragmental structure, Jie Wang et al. [46] fabricated a TENG with a cushioned Cu electrode and a contact area smaller than conventional TENG to improve the contact intimacy, which is shown in **Figure 5a**. After working in high-vacuum environment ($\sim 10^{-6}$ Torr), the triboelectric charge density is increased up to $660 \mu\text{C m}^{-2}$ (**Figure 5b**). Meanwhile, by properly combining the surface polarization from triboelectrification and residual dielectric polarization of ferroelectric materials, the surface charge density can be expected to further increase. Then, a TENG with the integration of triboelectric material PTFE with ferroelectric material BT (one type of doped barium titanate material) in vacuum is fabricated (**Figure 5c**), and its surface charge density jumped to $1003 \mu\text{C m}^{-2}$ without the constraint of air breakdown (**Figure 5d**). The surface polarization from triboelectrification induces the dielectric polarization in BT, and the latter further enhances the former until a new equilibrium rebuilds again. This combination of surface polarization and dielectric polarization greatly enhances the triboelectric charge density under the rest cycles of TENG. This work proposes a new optimized method to realize high-output power density TENG and meanwhile avoids the effect of environmental factors on the output performance of TENG.

4. Applications of air breakdown in conventional TENGs

TENGs can convert all kinds of mechanical energy into electricity, and have a built-in characteristic, that is high output voltage. Taking advantage of the high-output voltage characteristic, a lot of practical applications of TENG have been

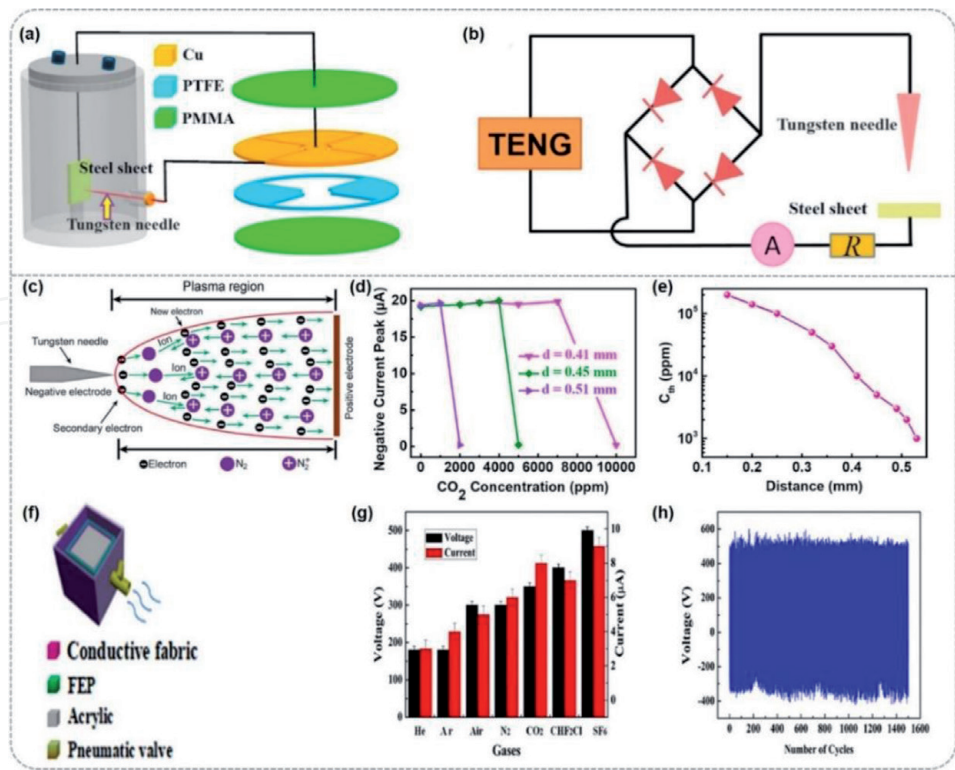


Figure 6. Self-powered gas sensors. (a) Structure diagram of the self-powered CO₂ sensor. (b) Circuit diagram of the self-powered CO₂ sensor. (c) Schematic image of the gas discharge process in pure N₂. (d) Under negative voltage, the curves of discharge current peak at different “d” under different CO₂ concentrations. (e) The curve of C_{th} at different “d” [49]. (f) Schematic diagram of the cubic-TENG structure. (g) Output performance under various gas atmospheres of He, Ar, air, N₂, CO₂, CHF₂Cl, and SF₆. (h) Long-term stability under an SF₆ atmosphere [55].

developed and successfully demonstrated in generating the input ions in mass spectrometry [51], fabricating electrospun nanofibers [52], driving field emission of electrons [53] etc. Considering the effects of gas composition and gas pressure on air breakdown, great efforts have been dedicated to study the air discharge for gas sensors. Ke Zhao et al. [54] fabricated a self-powered CO₂ gas sensor based on gas discharge induced by a TENG. The structure diagram of a self-powered CO₂ gas sensor is shown in **Figure 6a**. **Figure 6b** is the circuit diagram of the self-powered CO₂ gas sensor. The detailed gas discharge process is shown in **Figure 6c**. N₂ molecules lose electrons under the bombardment of electrons to form positive N₂ ions. N₂ molecules and electrons are accelerated to different directions under the electric field. Since the mass of positive N₂ ions is much higher than that of the electrons, electrons are easier to be accelerated. The accelerated electrons will bombard other N₂ molecules to form new positive ions and electrons; eventually an electron avalanche is formed. It is shown that the C_{th} (C_{th} is defined as the critical CO₂ concentration that causes the stop of gas discharge) decreased with the increase of distance. Shasha Lv et al. [55] fabricated an enclosed cubic-TENG consisting of an inner and outer box using a fluorinated ethylene propylene thin film and a layer of conducting fabric as the triboelectric layers, which is shown in **Figure 6f**. The output performance of the cubic-TENG in different gas atmospheres is shown in **Figure 6g**. Long-term stability under SF₆ atmosphere is shown in **Figure 6h**, indicating the potential of cubic-TENG as an energy-harvesting device and vibration sensor.

5. Mechanical energy harvesting via air breakdown

5.1 DC-TENG

Besides the applications of air breakdown in TENGs for gas sensors, some works about using air breakdown producing electricity also have been studied. Ya Yang et al. [56] fabricated a DC triboelectric generator (DC-TEG) consisting of two wheels and a belt, which is shown in **Figure 7a**. **Figure 7b** is a scanning electron microscope (SEM) image of the surface of PTFE. The working mechanism of the DC-TEG is illustrated in **Figure 7c** (The reference point T was used to monitor the relative sliding length of the belt). The design of the DC-TEG relied on the different properties to lose electrons, which is $\alpha_{III} > \alpha_I > \alpha_{II}$ in this structure. Here, the three materials are an Al wheel, a rubber belt, and a PTFE wheel. When the belt I makes contact with the wheel III, electrons will transfer from wheel III to belt I, resulting in net negative charges on the inner surface of belt I. After belt I makes contact with wheel II, electrons will transfer from belt I to wheel II. With the rotation of two wheels, more and more positive and negative charges will accumulate on the surface of wheel III and wheel II. Moreover, some positive charges are accumulated at electrode 2 (E2) due to electrostatic induction. So, the high electric field between wheel II and E2 will breakdown the air during the gap forming a pulsed DC output in external circuit. This DC-TEG exhibited good performance with different rotation rates and was demonstrated to power electronic systems directly. **Figure 7d** shows 1020 LEDs in series to fabricate LED panels. All the LEDs can be driven by the DC-TEG at a rotation speed of 3044 r min⁻¹ as shown in **Figure 7e**. **Figure 7f** depicts charging curves of a 1-μF capacitor charged by the DC-TEG at different rotation rates. The constant-current discharging curves of a 1000-μF capacitor after being charged by DC-TEG is shown in **Figure 7g**, where the discharging current is 60 μA.

Jianjun Luo et al. [57] reported a DC-TENG realized by air breakdown-induced ionized air channel. The structure of the DC-TENG is illustrated in **Figure 8a**. This DC-TENG is composed of a top triboelectric aluminum (Al) electrode (noted as

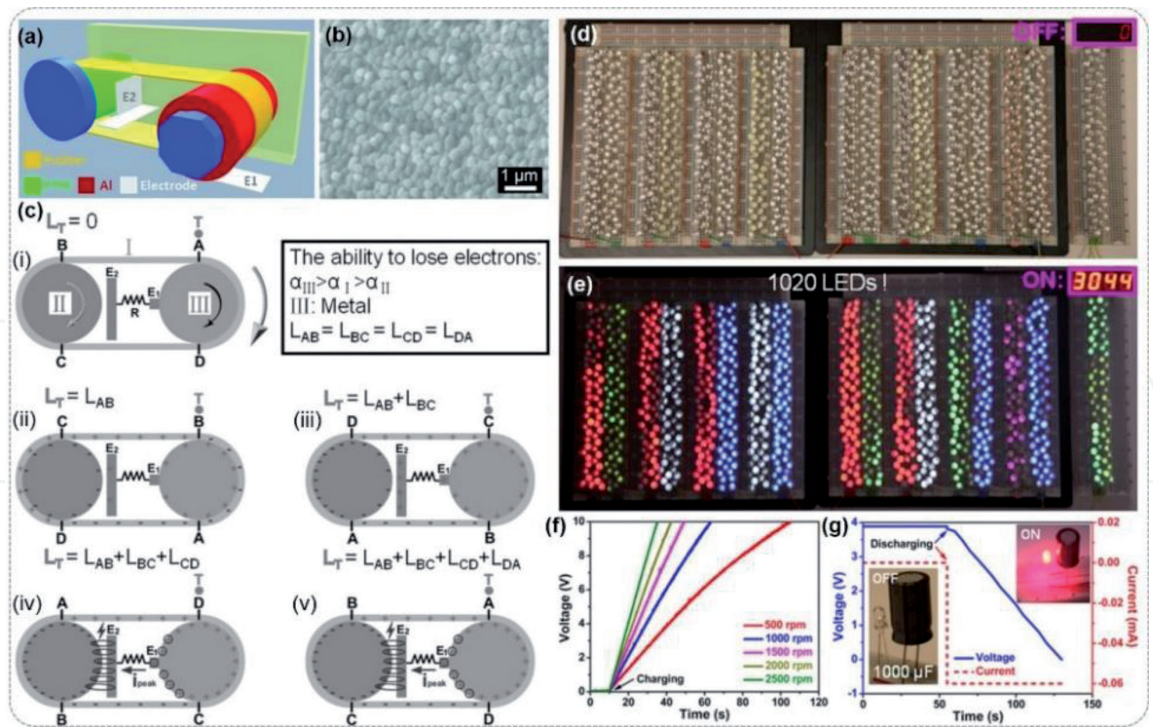


Figure 7. DC-TEG. (a) Schematic diagram of the DC-TEG. (b) SEM image of the PTFE surface. (c) Working mechanism of the DC-TEG. (i) Initial status without sliding motion of the belt. (ii–v) The triboelectric charge distributions when belt I went through the point T with the length of L_{AB} , $L_{AB} + L_{BC}$, $L_{AB} + L_{BC} + L_{CD}$, and $L_{AB} + L_{BC} + L_{CD} + L_{DA}$, respectively. L_T is the length that the belt went through the reference point T. L_{AB} is the length of the belt between A and B. (d), (e) Photographs of 1020 LEDs driven by the DC-TEG as a direct power source when the DC-TEG is (d) off and (e) on at a rotational speed of 3044 r min^{-1} . (f) The measured voltage of the DC-TEG charges a $1\text{-}\mu\text{F}$ capacitor at different rotational speeds. (g) The constant-current discharging curves of a $1000\text{-}\mu\text{F}$ capacitor after charging by the DC-TEG (inset shows the photographs of a red LED powered by the charged capacitor) [56].

Al-I), a sponge as a compression layer, a FEP film adhered to a back Al electrode (noted as Al-II), and an Al electrode at the bottom right corner (noted as Al-III). **Figure 8b** is the photograph of the DC-TENG. **Figure 8c,d** shows the transferred charges and short-circuit current of the DC-TENG with DC output characteristic. Using polydimethylsiloxane (PDMS), Kapton, and polyethylene terephthalate (PET) as triboelectric layers to replace FEP, the output characteristic is not changed, indicating the DC output is universal (**Figure 8e**). The working mechanism of the DC-TENG is illustrated in **Figure 8f**. The charge transfer between the top electrode and the dielectric layer is based on triboelectrification. In a working process, the electrons transport from bottom electrode to top electrode relying on an external circuit, which is Al-III in this structure. Then, the electrons flow back from top electrode to bottom electrode via the ionized air channel created by air breakdown. Because the inner flow of electrons based on air breakdown is in a single direction, the output current will be pulsed DC. This working mechanism was verified by real-time electrode potential monitoring, photocurrent signal detection, and controllable discharging observation. A flexible DC-TENG also fabricated to demonstrate this device can drive electronics directly without a rectifier, and the circuit diagram is illustrated in **Figure 8g**. **Figure 8h** shows the voltage curves of a $1\text{-}\mu\text{F}$ capacitor charged by the DC-TENG at different frequencies. The DC-TENG can also integrate with a capacitor and a calculator to form a self-powered system (**Figure 8i**).

5.2 Constant-current TENG arising from electrostatic breakdown

TENGs are considered as a potential solution via building self-powered systems. The conventional TENGs have two built-in characteristics (i.e., AC consisted of

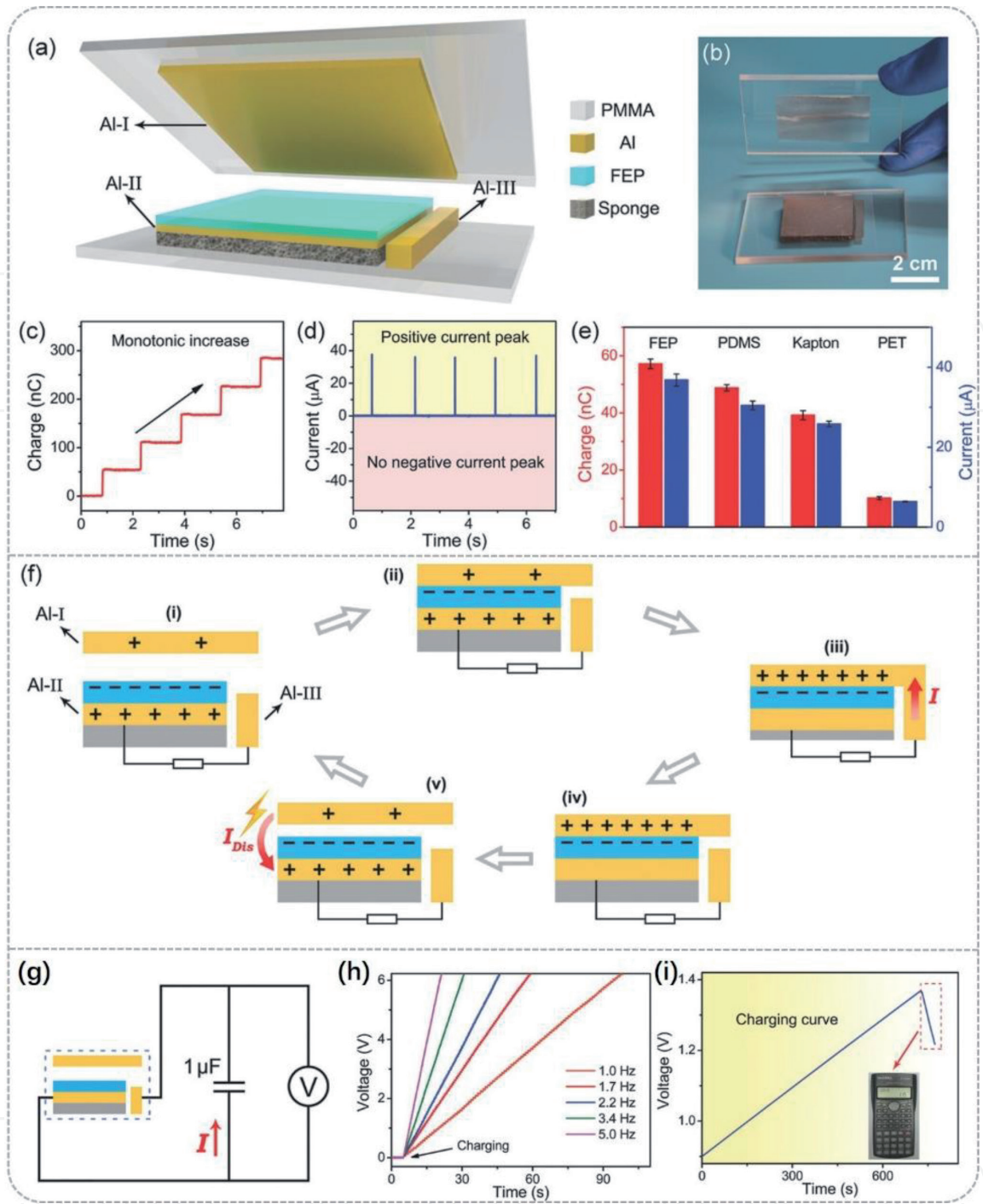


Figure 8. DC-TENG. (a) Structure of the DC-TENG. (b) Photograph of the DC-TENG. (c) Transferred charges of the DC-TENG. (d) Short-circuit current of the DC-TENG. (e) Output performance of DC-TENG using different triboelectric materials. (f) Schematic working principle of the DC-TENG achieved through the ionized air channel caused by air breakdown. (g) Circuit diagram of a 1- μF capacitor directly and continuously charged by the DC-TENG without a rectifier. (h) Measured voltage of a 1- μF capacitor charged by the DC-TENG at different frequencies. (i) Charging curve of a 1000- μF capacitor charged by the flexible multilayered DC-TENG (inset shows the photograph of a calculator powered by the charged capacitor). (i-v) The working mechanism of the DC-TENG in stable working state [57].

pulse series). Generally, TENGs need to connect with a rectifier or a capacitor to drive electronics, which takes away its portability advantage [58, 59]. Second, the pulsed output current of TENGs result in high crest factor, which is a key metric to output instability defined as the ratio of the peak value to the root mean square value. This greatly influences their performance for energy storage efficiency and powering electronics [59]. In addition, triboelectric charge density as one of the key properties of TENGs has been greatly increased; therefore, a very high

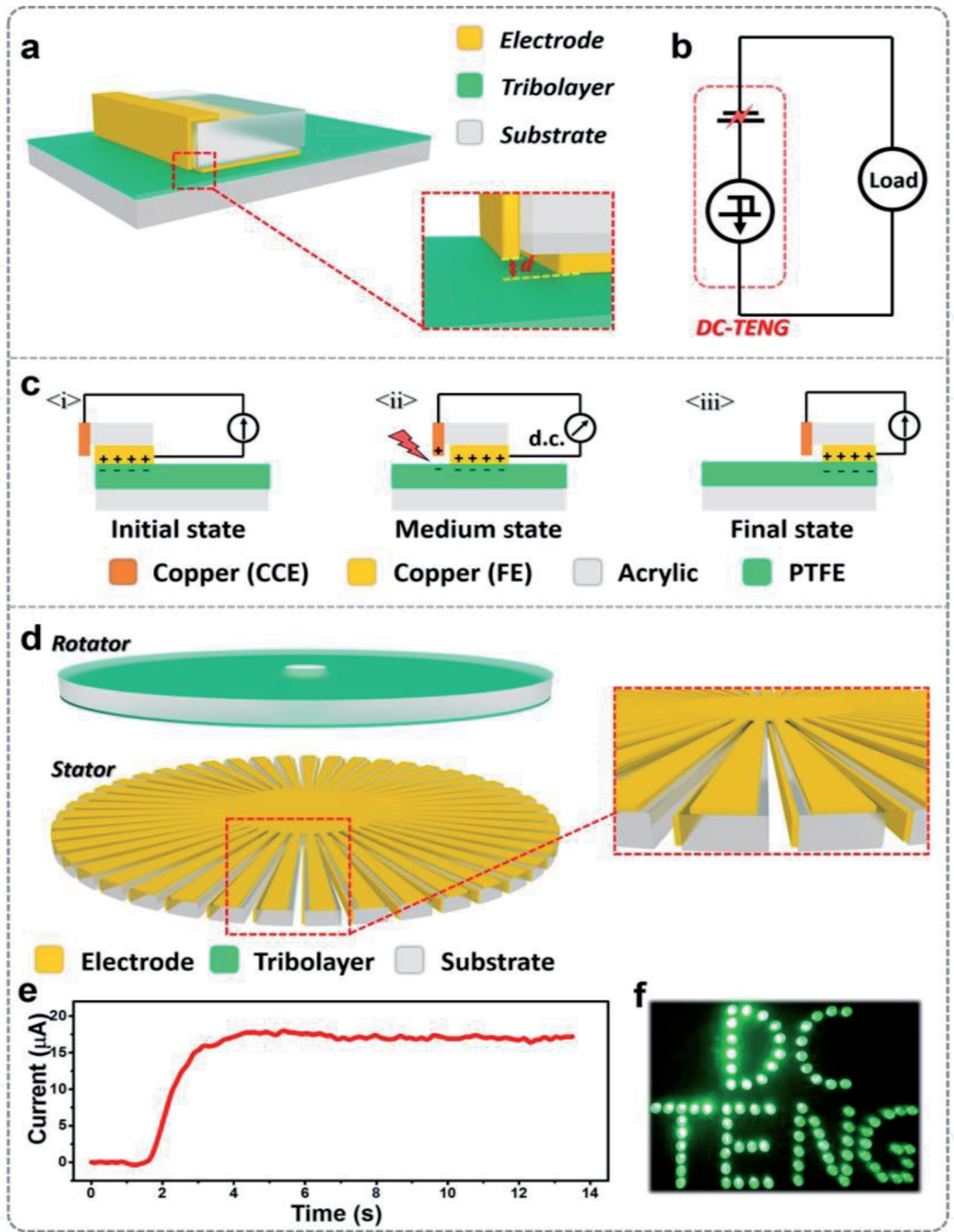


Figure 9. Constant-current TENG. (a) A schematic illustration of the sliding mode DC-TENG. (b) Equivalent circuit model of the DC-TENG. (c) Working mechanism of the sliding mode DC-TENG in full cyclic motion. (d) Structural design of the rotary mode DC-TENG. Inset shows a zoomed-in illustration of its stator. (e) Constant current output of the DC-TENG. (f) Photograph of 81 LEDs with stable luminance powered by a rotary mode DC-TENG [60].

electrostatic field will be built in TENG, which also leads to air breakdown and results in unwanted charge quantity loss and, consequently, quadratic loss in output power. The charge quantity loss can be roughly estimated with its charge density gap in air and vacuum. With a 50- μm PTFE film as a triboelectric layer, $240\text{ }\mu\text{C m}^{-2}$ is the theoretical upper limit in air [39, 44], but $1003\text{ }\mu\text{C m}^{-2}$ has been achieved in vacuum, where a dominant part is wasted because of air breakdown [46].

To harvest energy during electrostatic breakdown, Jie Wang et al. [60] designed a next-generation DC-TENG via the triboelectrification effect and electrostatic

breakdown, which consists of a frictional electrode (FE), a charge collecting electrode (CCE), and a triboelectric layer (**Figure 9a**). The CCE layer is fixed on the side of a sliding acrylic substrate, with a subtle distance to the triboelectric layer, which is a PTFE layer attached to another acrylic sheet. The CCE and FE both are copper electrodes here. The physics model of the new DC-TENG is made up of an electric charge source and a broken-down capacitor composed of the CCE and PTFE film, as its equivalent circuit briefly demonstrates in **Figure 9b**. It is different with a conventional TENG, whose paradigm is a variable capacitor initially charged by triboelectrification and generating AC pluses by electrostatic induction. The working mechanism of the DC-TENG is shown in **Figure 9c**. When the FE makes contact with the PTFE, electrons will transfer from the FE to PTFE based on triboelectrification effect. PTFE as an electret can hold a quasi-permanent electric charge (**Figure 9c, i**). Thus, when the slider moves forward, the electrons on the surface of PTFE will build a very high electric field between the negatively charged PTFE film and the CCE. As long as it exceeds the dielectric strength of the air between them, whose value is approximately 3 kV/mm from Paschen's law, it can cause the nearby air to partially ionize and begin conducting. Electrons will transfer from PTFE film to CCE (**Figure 9c, ii**); that is, the CCE is rationally placed to induce air breakdown, creating artificial lightning. When the slider is stationary on the surface of PTFE, electrons will stop transfer (**Figure 9c, iii**). Because the inner flow direction of electrons is fixed from the FE to the PTFE film and then to the CCE, the output electrons will also be in a single direction, that is, from the CCE to the FE. Thus, cyclic DC can be produced by periodically sliding the slider.

To optimize the output performance, a radially arrayed rotary of DC-TENG is fabricated by parallel multiple DC-TENGs, which is shown in **Figure 9d** and inset shows a zoomed-in illustration of its stator. When the motor rotates steadily, the crest factor of output current is very close to 1, indicating approximately constant current output characteristic (**Figure 9e**). This DC-TENG was demonstrated to charge capacitors or drive electronics without a rectifier. A light-emitting diode (LED) bulb arrays can also be lit up by the rotary mode DC-TENG with a rotation rate of 500 r min^{-1} (**Figure 9f**). Unlike when driven by the conventional AC-TENG, the LEDs remain at constant luminance without flashing lights.

6. Conclusions

Harvesting of environmental mechanical energy as an eco-friendly energy generation method is particularly a promising solution and plays an increasingly important role in driving wearable electronics and sensor networks in the IoTs. Based on the triboelectrification effect and electrostatic induction, the use of TENG invented in 2012 by Zhong Lin Wang has been demonstrated as a cost-effective, clean, and sustainable strategy to convert mechanical energy into electricity with comprehensive advantages of light-weight, small size, a wide choice of materials, and high efficiency even at low frequencies, which shows great potential in promoting the miniaturization trend of self-powered systems. With the gradually increase in triboelectric charge density, electrostatic breakdown, which is generally considered as a negative effect in the conventional TENG, becomes an issue that must to be considered. The theoretical and experimental studies of air breakdown in TENGs are important to promote the development of this field. By taking advantage of the electrostatic discharge, several types of DC-TENG have been demonstrated to power electronics directly without a rectifier or a capacitor. Comparing with the output characteristics of conventional TENG (AC consisted of pulse series), a constant-current output (crest factor ~ 1) is achieved by coupling triboelectrification

effect and electrostatic breakdown. This constant-current TENG has been demonstrated to drive LED bulb arrays that remain at constant luminance without flashing lights. Moreover, it can not only promote the miniaturization trend of TENG and self-powered systems but also provide a paradigm shifting technique to in situ gain electrical energy. Based on the above discussion and analysis, the electrostatic breakdown in TENG will soon become a hot issue and we would require new studies in electrostatic breakdown.

Acknowledgements

The authors would like to thank the financial supports from the National Key R& D Project from Minister of Science and Technology (2016YFA0202704) and National Natural Science Foundation of China (Grant Nos. 61774016, 21773009, 51432005, 5151101243, 51561145021).

Conflict of interest

There is no conflict of interest.

Author details

Jie Wang^{1,2*}, Di Liu^{1,2}, Linglin Zhou^{1,2} and Zhong Lin Wang^{1,2,3}

1 Beijing Institute of Nanoenergy and Nanosystems, Chinese Academy of Sciences, Beijing, P. R. China

2 College of Nanoscience and Technology, University of Chinese Academy of Sciences, Beijing, P. R. China

3 School of Materials Science and Engineering, Georgia Institute of Technology, Atlanta, GA, USA

*Address all correspondence to: wangjie@binn.cas.cn

IntechOpen

© 2019 The Author(s). Licensee IntechOpen. This chapter is distributed under the terms of the Creative Commons Attribution License (<http://creativecommons.org/licenses/by/3.0>), which permits unrestricted use, distribution, and reproduction in any medium, provided the original work is properly cited. 

References

- [1] Ballou JW. Static electricity in textiles. *Textile Research Journal*. 1954;**24**(2):146-155. DOI: 10.1177/004051755402400209
- [2] Shashoua VE. Static electricity in polymers. 1. Theory and measurement. *Journal of Polymer Science*. 1958;**33**(126):65-85. DOI: 10.1002/pol.1958.1203312608
- [3] Shashoua VE. Static electricity in polymers. 2. Chemical structure and antistatic behavior. *Journal of Polymer Science Part A: General Papers*. 1963;**1**(1):169-187. DOI: 10.1002/pol.1963.100010114
- [4] Lowell J, Roseinnes AC. Contact electrification. *Advances in Physics*. 1980;**29**(6):947-1023. DOI: 10.1080/00018738000101466
- [5] Terris BD, Stern JE, Rugar D, Mamin HJ. Contact electrification using force microscopy. *Physical Review Letters*. 1989;**63**(24):2669-2672. DOI: 10.1103/PhysRevLett.63.2669
- [6] Baytekin HT, Patashinski AZ, Branicki M, Baytekin B, Soh S, Grzybowski BA. The mosaic of surface charge in contact electrification. *Science*. 2011;**333**(6040):308-312. DOI: 10.1126/science.1201512
- [7] Horn RG, Smith DT. Contact electrification and adhesion between dissimilar materials. *Science*. 1992;**256**(5055):362-364. DOI: 10.1126/science.256.5055.362
- [8] Lacks DJ, Sankaran RM. Contact electrification of insulating materials. *Journal of Physics D: Applied Physics*. 2011;**44**(45):453001. DOI: 10.1088/0022-3727/44/45/453001
- [9] Talawar MB, Agrawal AP, Anniyappan M, Wani DS, Bansode MK, Gore GM. Primary explosives: Electrostatic discharge initiation, additive effect and its relation to thermal and explosive characteristics. *Journal of Hazardous Materials*. 2006;**137**(2):1074-1078. DOI: 10.1016/j.jhazmat.2006.03.043
- [10] Greason WD. Electrostatic discharge—A charge driven phenomenon (reprinted from electrical overstress electrostatic discharge symposium proceedings, Eos-13, Las-Vegas, Nv, Usa, September 24-26, 1991). *Journal of Electrostatics*. 1992;**28**(3):199-218. DOI: 10.1016/0304-3886(92)90073-3
- [11] Kasemir HW. A contribution to the electrostatic theory of a lightning discharge. *Journal of Geophysical Research*. 1960;**65**(7):1873-1878. DOI: 10.1029/JZ065i007p01873
- [12] Voldman SH. ESD: Physics and Devices[M]. England: John Wiley & Sons; 2005
- [13] Voldman SH. Lightning rods for nanoelectronics[J]. *Scientific American*. 2002;**287**(4):90-97
- [14] Vinson JE, Liou JJ. Electrostatic discharge in semiconductor devices: An overview. *Proceedings of the IEEE*. 1998;**86**(2):399-418. DOI: 10.1109/5.659493
- [15] Ker MD, Hsu KC. Overview of on-chip electrostatic discharge protection design with SCR-based devices in CMOS integrated circuits. *IEEE Transactions on Device and Materials Reliability*. 2005;**5**(2):235-249. DOI: 10.1109/tdmr.2005.846824
- [16] Voldman SH. The state of the art of electrostatic discharge protection: Physics, technology, circuits, design, simulation, and scaling. *IEEE Journal of Solid-State Circuits*. 1999;**34**(9):1272-1282. DOI: 10.1109/4.782088

- [17] Wallash A, Kim YK. Magnetic changes in GMR heads caused by electrostatic discharge. *IEEE Transactions on Magnetics*. 1998;**34**(4):1519-1521. DOI: 10.1109/20.706602
- [18] Voldman SH. *ESD: Failure Mechanisms and Models*[M]. United Kingdom: John Wiley & Sons; 2009
- [19] Voldman SH. *Electrical Overstress (EOS): Devices, Circuits and Systems*[M]. United Kingdom: John Wiley & Sons; 2013
- [20] Voldman SH. *ESD: Circuits and Devices*[M]. England: John Wiley & Sons; 2015
- [21] Wang ZL. Entropy theory of distributed energy for internet of things. *Nano Energy*. 2019;**58**:669-672. DOI: 10.1016/j.nanoen.2019.02.012
- [22] Larcher D, Tarascon JM. Towards greener and more sustainable batteries for electrical energy storage. *Nature Chemistry*. 2015;**7**(1):19-29. DOI: 10.1038/nchem.2085
- [23] Law M, Greene LE, Johnson JC, Saykally R, Yang PD. Nanowire dye-sensitized solar cells. *Nature Materials*. 2005;**4**(6):455-459. DOI: 10.1038/nmat1387
- [24] Foley AM, Leahy PG, Marvuglia A, McKeogh EJ. Current methods and advances in forecasting of wind power generation. *Renewable Energy*. 2012;**37**(1):1-8. DOI: 10.1016/j.renene.2011.05.033
- [25] Kraemer D, Poudel B, Feng HP, Caylor JC, Yu B, Yan X, et al. High-performance flat-panel solar thermoelectric generators with high thermal concentration. *Nature Materials*. 2011;**10**(7):532-538. DOI: 10.1038/nmat3013
- [26] Wang ZL, Song JH. Piezoelectric nanogenerators based on zinc oxide nanowire arrays. *Science*. 2006;**312**(5771):242-246. DOI: 10.1126/science.1124005
- [27] Zhu G, Chen J, Zhang TJ, Jing QS, Wang ZL. Radial-arrayed rotary electrification for high performance triboelectric generator. *Nature Communications*. 2014;**5**:3426. DOI: 10.1038/ncomms4426
- [28] Jing QS, Xie YN, Zhu G, Han RPS, Wang ZL. Self-powered thin-film motion vector sensor. *Nature Communications*. 2015;**6**:8031. DOI: 10.1038/ncomms9031
- [29] Wang SH, Lin L, Wang ZL. Triboelectric nanogenerators as self-powered active sensors. *Nano Energy*. 2015;**11**:436-462. DOI: 10.1016/j.nanoen.2014.10.034
- [30] Niu SM, Wang XF, Yi F, Zhou YS, Wang ZL. A universal self-charging system driven by random biomechanical energy for sustainable operation of mobile electronics. *Nature Communications*. 2015;**6**:8975. DOI: 10.1038/ncomms9975
- [31] Fan FR, Tian ZQ, Wang ZL. Flexible triboelectric generator. *Nano Energy*. 2012;**1**(2):328-334. DOI: 10.1016/j.nanoen.2012.01.004
- [32] Wang ZL. On Maxwell's displacement current for energy and sensors: The origin of nanogenerators. *Materials Today*. 2017;**20**(2):74-82. DOI: 10.1016/j.mattod.2016.12.001
- [33] Wang ZL. Triboelectric nanogenerators as new energy technology and self-powered sensors—Principles, problems and perspectives. *Faraday Discussions*. 2014;**176**:447-458. DOI: 10.1039/C4FD00159A

- [34] Zi YL, Lin L, Wang J, Wang SH, Chen J, Fan X, et al. Triboelectric-pyroelectric-piezoelectric hybrid cell for high-efficiency energy-harvesting and self-powered sensing. *Advanced Materials*. 2015;27(14):2340-2347. DOI: 10.1002/adma.201500121
- [35] Wen Z, Yeh MH, Guo HY, Wang J, Zi YL, Xu WD, et al. Self-powered textile for wearable electronics by hybridizing fiber-shaped nanogenerators, solar cells, and supercapacitors. *Science Advances*. 2016;2(10):e1600097. DOI: 10.1126/sciadv.1600097
- [36] Wang J, Li XH, Zi YL, Wang SH, Li ZL, Zheng L, et al. A flexible fiber-based supercapacitor-triboelectric-nanogenerator power system for wearable electronics. *Advanced Materials*. 2015;27(33):4830-4836. DOI: 10.1002/adma.201501934
- [37] Guo HY, Pu XJ, Chen J, Meng Y, Yeh MH, Liu GL, et al. A highly sensitive, self-powered triboelectric auditory sensor for social robotics and hearing aids. *Science robotics*. 2018;3(20):eaat2516. DOI: 10.1126/scirobotics.aat2516
- [38] Cheng P, Guo HY, Wen Z, Zhang CL, Yin X, Li XY, et al. Largely enhanced triboelectric nanogenerator for efficient harvesting of water wave energy by soft contacted structure. *Nano Energy*. 2019;57:432-439. DOI: 10.1016/j.nanoen.2018.12.054
- [39] Wang SH, Xie YN, Niu SM, Lin L, Liu C, Zhou YS, et al. Maximum surface charge density for triboelectric nanogenerators achieved by ionized-air injection: Methodology and theoretical understanding. *Advanced Materials*. 2014;26(39):6720-6728. DOI: 10.1002/adma.201402491
- [40] Zi YL, Niu SM, Wang J, Wen Z, Tang W, Wang ZL. Standards and figure-of-merits for quantifying the performance of triboelectric nanogenerators. *Nature Communications*. 2015;6:8376. DOI: 10.1038/ncomms9376
- [41] Wang J, Wen Z, Zi YL, Zhou PF, Lin J, Guo HY, et al. All-plastic-materials based self-charging power system composed of triboelectric nanogenerators and supercapacitors. *Advanced Functional Materials*. 2016;26(7):1070-1076. DOI: 10.1002/adfm.201504675
- [42] Yin X, Liu D, Zhou LL, Li XY, Zhang CL, Cheng P, et al. Structure and dimension effects on the performance of layered triboelectric nanogenerators in contact-separation mode. *ACS Nano*. 2019;13(1):698-705. DOI: 10.1021/acsnano.8b07935
- [43] Wang SH, Zi YL, Zhou YS, Li SM, Fan FR, Lin L, et al. Molecular surface functionalization to enhance the power output of triboelectric nanogenerators. *Journal of Materials Chemistry A*. 2016;4(10):3728-3734. DOI: 10.1039/c5ta10239a
- [44] Wang J, Li SM, Yi F, Zi YL, Lin J, Wang XF, et al. Sustainably powering wearable electronics solely by biomechanical energy. *Nature Communications*. 2016;7:12744. DOI: 10.1038/ncomms12744
- [45] Chun JS, Ye BU, Lee JW, Choi D, Kang CY, Kim SW, et al. Boosted output performance of triboelectric nanogenerator via electric double layer effect. *Nature Communications*. 2016;7:12985. DOI: 10.1038/ncomms12985
- [46] Wang J, Wu CS, Dai YJ, Zhao ZH, Wang A, Zhang TJ, et al. Achieving ultrahigh triboelectric charge density for efficient energy harvesting. *Nature Communications*. 2017;8:88. DOI: 10.1038/s41467-017-00131-4
- [47] Su ZM, Han MD, Cheng XL, Chen HT, Chen XX, Zhang HX. Asymmetrical

triboelectric nanogenerator with controllable direct electrostatic discharge. *Advanced Functional Materials*. 2016;**26**(30):5524-5533. DOI: 10.1002/adfm.201600909

[48] Zi YL, Wu CS, Ding WB, Wang ZL. Maximized effective energy output of contact-separation triggered triboelectric nanogenerators as limited by air breakdown. *Advanced Functional Materials*. 2017;**27**(24):1700049. DOI: 10.1002/adfm.201700049

[49] Xu ZS, Duan JJ, Li WB, Wu N, Pan Y, Lin SZ, et al. Boosting the efficient energy output of electret nanogenerators by suppressing air breakdown under ambient conditions. *ACS Applied Materials & Interfaces*. 2019;**11**(4):3984-3989. DOI: 10.1021/acsami.8b19599

[50] Jiang C, Dai KR, Yi F, Han YZ, Wang XF, You Z. Optimization of triboelectric nanogenerator load characteristics considering the air breakdown effect. *Nano Energy*. 2018;**53**:706-715. DOI: 10.1016/j.nanoen.2018.09.036

[51] Li AY, Zi YL, Guo HY, Wang ZL, Fernandez FM. Triboelectric nanogenerators for sensitive nano-coulomb molecular mass spectrometry. *Nature Nanotechnology*. 2017;**12**(5):481-487. DOI: 10.1038/nnano.2017.17

[52] Li CJ, Yin YY, Wang B, Zhou T, Wang JN, Luo JJ, et al. Self-powered electrospinning system driven by a triboelectric nanogenerator. *ACS Nano*. 2017;**11**(10):10439-10445. DOI: 10.1021/acsnano.7b05626

[53] Zi YL, Wu CS, Ding WB, Wang XF, Dai YJ, Cheng J, et al. Field emission of electrons powered by a triboelectric nanogenerator. *Advanced Functional Materials*. 2018;**28**(21):1800610. DOI: 10.1002/adfm.201800610

[54] Zhao K, Gu GQ, Zhang YN, Zhang B, Yang F, Zhao L, et al. The

self-powered CO₂ gas sensor based on gas discharge induced by triboelectric nanogenerator. *Nano Energy*. 2018;**53**:898-905. DOI: 10.1016/j.nanoen.2018.09.057

[55] Lv SS, Yu B, Huang T, Yu H, Wang HZ, Zhang QH, et al. Gas-enhanced triboelectric nanogenerator based on fully-enclosed structure for energy harvesting and sensing. *Nano Energy*. 2019;**55**:463-469. DOI: 10.1016/j.nanoen.2018.11.022

[56] Yang Y, Zhang HL, Wang ZL. Direct-current triboelectric generator. *Advanced Functional Materials*. 2014;**24**(24):3745-3750. DOI: 10.1002/adfm.201304295

[57] Luo JJ, Xu L, Tang W, Jiang T, Fan FR, Pang YK, et al. Direct-current triboelectric nanogenerator realized by air breakdown induced ionized air channel. *Advanced Energy Materials*. 2018;**8**(27):1800889. DOI: 10.1002/aenm.201800889

[58] Zhu XX, Li ZB, Li XS, Su L, Wei XY, Kuang SY, et al. Triboelectrification-enabled thin-film tactile matrix for self-powered high-resolution imaging. *Nano Energy*. 2018;**50**:497-503. DOI: 10.1016/j.nanoen.2018.05.061

[59] Ryu H, Lee JH, Khan U, Kwak SS, Hinchet R, Kim SW. Sustainable direct current powering a triboelectric nanogenerator via a novel asymmetrical design. *Energy & Environmental Science*. 2018;**11**(8):2057-2063. DOI: 10.1039/c8ee00188j

[60] Liu D, Yin X, Guo H, Zhou L, Li X, Zhang C, et al. A constant-current triboelectric nanogenerator arising from electrostatic breakdown. *Science Advances*. 2019;**5**(4):eaav6437. DOI: 10.1126/sciadv.aav6437